University of Texas Rio Grande Valley

ScholarWorks @ UTRGV

Physics and Astronomy Faculty Publications and Presentations

College of Sciences

2020

Monitoring of the radio galaxy M 87 during a low-emission state from 2012 to 2015 with MAGIC

Juan P. Madrid
The University of Texas Rio Grande Valley, juan.madrid@utrgv.edu

Follow this and additional works at: https://scholarworks.utrgv.edu/pa_fac

Part of the Astrophysics and Astronomy Commons, and the Physics Commons

Recommended Citation

Monitoring of the radio galaxy M 87 during a low-emission state from 2012 to 2015 with MAGIC

MAGIC Collaboration: V. A. Acciari,[1] S. Ansoldi,[2,3] L. A. Antonelli,[4]
A. Arbet Engels,[5] C. Arcaro,[6,7]★ D. Baack,[8] A. Babić,[9] B. Banerjee,[10] P. Bangale,[11]★
U. Barres de Almeida,[12] J. A. Barrio,[13] J. Becerra González,[1] W. Bednarek,[14]
L. Bellizzi,[15] E. Bernardini,[16,17] A. Berti,[18] J. Besenrieder,[11] W. Bhattacharyya,[16]
C. Bigongiari,[4] A. Biland,[5] O. Blanch,[19] G. Bonnoli,[15] Ž. Bošnjak,[9] G. Busetto,[17]
R. Carosi,[20] G. Ceribella,[11] Y. Chai,[11] A. Chilingaryan,[21] S. Cikota,[9] S. M. Colak,[19]
U. Colin,[11] E. Colombo,[1] J. L. Contreras,[13] J. Cortina,[22] S. Covino,[4] V. D'Elia,[4]
P. Da Vela,[20] F. Dazzi,[4] A. De Angelis,[17] B. De Lotto,[2] M. Delfino,[19,23] J. Delgado,[19,23]
D. Depaoli,[18] F. Di Pierro,[18] L. Di Venere,[18] E. Do Souto Espiñeira,[19]
D. Dominis Prester,[9] A. Donini,[2] D. Dorner,[24] M. Doro,[17] D. Elsaesser,[8]
V. Fallah Ramazani,[25] A. Fattorini,[8] A. Fernández-Barral,[17] G. Ferrara,[4] D. Fidalgo,[13]
L. Foffano,[17] M. V. Fonseca,[13] L. Font,[26] C. Fruck,[11] S. Fukami,[3] R. J. García López,[1]
M. Garczarczyk,[16] S. Gasparyan,[21] M. Gaug,[26] N. Giglietto,[18] F. Giordano,[18]
N. Godinović,[9] D. Green,[11] D. Guberman,[19] D. Hadasch,[3] A. Hahn,[11] J. Herrera,[1]
J. Hoang,[13] D. Hrupec,[9] M. Hütten,[11] T. Inada,[3] S. Inoue,[3] K. Ishio,[11] Y. Iwamura,[3]
L. Jouvin,[19] D. Kerszberg,[19] H. Kubo,[3] J. Kushida,[3] A. Lamastra,[4] D. Lelas,[9] F. Leone,[4]
E. Lindfors,[25] S. Lombardi,[4] F. Longo,[2,27] M. López,[13] R. López-Coto,[17]
A. López-Oramas,[1] S. Loporchio,[18] B. Machado de Oliveira Fraga,[12] C. Maggio,[26]
P. Majumdar,[10] M. Makariev,[28] M. Mallamaci,[17] G. Maneva,[28] M. Manganaro⬤,[9]★
K. Mannheim,[24] L. Maraschi,[4] M. Mariotti,[17] M. Martínez,[19] S. Masuda,[3]
D. Mazin,[3,11]★ S. Mićanović,[9] D. Miceli,[2] M. Minev,[28] J. M. Miranda,[15] R. Mirzoyan,[11]
E. Molina,[29] A. Moralejo,[19] D. Morcuende,[13] V. Moreno,[26] E. Moretti,[19]
P. Munar-Adrover,[26] V. Neustroev,[25] C. Nigro,[16] K. Nilsson,[25] D. Ninci,[19]
K. Nishijima,[3] K. Noda,[3] L. Nogués,[19] M. Nöthe,[8] S. Nozaki,[3] S. Paiano,[17] J. Palacio,[19]
M. Palatiello,[2] D. Paneque,[11] R. Paoletti,[15] J. M. Paredes,[29] P. Peñil,[13] M. Peresano,[2]
M. Persic,[2,30] P. G. Prada Moroni,[20] E. Prandini,[17] I. Puljak,[9] W. Rhode,[8] M. Ribó,[29]
J. Rico,[19] C. Righi,[4] A. Rugliancich,[20] L. Saha,[13] N. Sahakyan,[21] T. Saito,[3] S. Sakurai,[3]
K. Satalecka,[16] K. Schmidt,[8] T. Schweizer,[11] J. Sitarek,[14] I. Šnidarić,[9] D. Sobczynska,[14]
A. Somero,[1] A. Stamerra,[4] D. Strom,[11] M. Strzys,[11] Y. Suda,[11] T. Surić,[9] M. Takahashi,[3]
F. Tavecchio,[4] P. Temnikov,[28] T. Terzić,[9] M. Teshima,[3,11] N. Torres-Albà,[29] L. Tosti,[18]
S. Tsujimoto,[3] V. Vagelli,[18] J. van Scherpenberg,[11] G. Vanzo,[1] M. Vazquez Acosta,[1]
C. F. Vigorito,[18] V. Vitale,[18] I. Vovk,[11] M. Will,[11] D. Zarić,[9] Collaborators: K. Asano,[31]
K. Hada,[32,33] D. E. Harris,[34]† M. Giroletti,[35] H. E. Jermak,[36] J. P. Madrid,[37]
F. Massaro,[38,39,40,41] S. Richter,[6] F. Spanier,[6,42] I. A. Steele[36] and R. C. Walker[43]

★ E-mail: contact.magic@mpp.mpg.de
† Deceased.

Affiliations are listed at the end of the paper

ABSTRACT

M 87 is one of the closest ($z = 0.004\,36$) extragalactic sources emitting at very high energies (VHE, $E > 100$ GeV). The aim of this work is to locate the region of the VHE gamma-ray emission and to describe the observed broad-band spectral energy distribution (SED) during the low VHE gamma-ray state. The data from M 87 collected between 2012 and 2015 as part of a MAGIC monitoring programme are analysed and combined with multiwavelength data from *Fermi*-LAT, *Chandra*, *HST*, EVN, VLBA, and the Liverpool Telescope. The averaged VHE gamma-ray spectrum can be fitted from $\sim$100 GeV to $\sim$10 TeV with a simple power law with a photon index of (-2.41 ± 0.07), while the integral flux above 300 GeV is (1.44 ± 0.13) $\times$ 10^{-12} cm^{-2} s^{-1}. During the campaign between 2012 and 2015, M 87 is generally found in a low-emission state at all observed wavelengths. The VHE gamma-ray flux from the present 2012–2015 M 87 campaign is consistent with a constant flux with some hint of variability ($\sim 3\sigma$) on a daily time-scale in 2013. The low-state gamma-ray emission likely originates from the same region as the flare-state emission. Given the broad-band SED, both a leptonic synchrotron self-Compton and a hybrid photohadronic model reproduce the available data well, even if the latter is preferred. We note, however, that the energy stored in the magnetic field in the leptonic scenario is very low, suggesting a matter-dominated emission region.

Key words: radiation mechanisms: non-thermal – galaxies: active – galaxies: individual: M 87 – galaxies: jets – gamma rays: galaxies.

1 INTRODUCTION

M 87 is a large elliptical radio galaxy of Fanaroff–Riley type I (FR I; Fanaroff & Riley 1974), located in the Virgo Cluster, at a distance of 16.4 ± 0.5 Mpc (Bird et al. 2010). M 87 is powered by a super-massive black hole with a mass assumed to be $(6.5 \pm 0.2_{\text{stat}} \pm 0.7_{\text{sys}}) \times 10^9$ M$_\odot$ (Gebhardt et al. 2011; Event Horizon Telescope Collaboration 2019b).

The relativistic jet of M 87 is misaligned with respect to our line of sight with an angle between $15°$ and $25°$ (Biretta, Sparks & Macchetto 1999; Acciari et al. 2009; Walker et al. 2018). The orientation and vicinity of M 87 allow the jet to be studied during its evolution, from the core to the extended lobe, where it slows down ending its path interacting with the intergalactic medium (Owen, Eilek & Kassim 2000). The jet extends for $\gtrsim$30 arcsec (Marshall et al. 2002), and several knots along its length have been resolved in radio, optical, and X-ray bands (Perlman et al. 2001; Wilson & Yang 2002; Kim et al. 2018a,b). The inner knot *HST*-1, located at 0.85 arcsec from the core, has been in a flaring state since 2000 (Harris et al. 2003; Waters & Zepf 2005; Harris et al. 2006), reaching the maximum flux in 2005 and had a secondary flaring in 2006–2007 (see Harris et al. 2009; Madrid 2009; Abramowski et al. 2012).

The temporal correlation between the very high energies (VHE, $E > 100$ GeV) gamma-ray emission and multiwavelength (MWL) data, in which the source is spatially resolved, provides a unique opportunity to locate the origin of VHE gamma-ray emission in active galactic nuclei (AGNs). M 87 was detected in TeV gamma rays first by the HEGRA (High-Energy-Gamma-Ray Astronomy) Collaboration in 1998 (Aharonian et al. 2003). The VERITAS (Very Energetic Radiation Imaging Telescope Array System) Collaboration reported a clear detection of M 87 in the 2007 campaign

at energies above 250 GeV (Acciari et al. 2008) and continued to routinely monitor the source (Acciari et al. 2010). The first detection of gamma-ray emission from M 87 with MAGIC (Major Atmospheric Gamma-ray Imaging Cherenkov) occurred in 2005 in a low-flux state, and results of those observations together with those performed between 2006 and 2007 were reported in Aleksić et al. (2012).

During a flare in 2008, detected through a monitoring campaign, MAGIC observed a flux variability on time-scales as short as a day (Acciari et al. 2008; Albert et al. 2008). As of 2019, M 87 has been monitored for more than 10 yr in the TeV band by MAGIC, H.E.S.S. (High Energy Stereoscopic System), and VERITAS (Acciari et al. 2009; Abramowski et al. 2012; Aliu et al. 2012; Beilicke & VERITAS Collaboration 2012). According to the available VHE gamma-ray data, a total of three periods of high activity occurred in 2005, 2008, and 2010.

The modelling of VHE gamma-ray emission in the context of the broad-band spectral energy distribution (SED) is challenging and draws the attention of several theory groups, see, e.g. Georganopoulos, Perlman & Kazanas (2005), Ghisellini, Tavecchio & Chiaberge (2005), Tavecchio & Ghisellini (2008), Istomin & Sol (2009), and Giannios, Uzdensky & Begelman (2010).

The low state of M 87 is important for modelling as it can be used to describe a 'baseline' state to be used as a reference, even if several model parameters remain unconstrained in the absence of flux variability. The study of the source in a high state can then be associated with the low-state reference improving the interpretation of the emission scenarios. Aleksić et al. (2012) previously modelled the low-state broad-band SED using the same model applied to the high states observed in 2008. De Jong et al. (2015) and Prieto et al. (2016) also studied the M 87 activity in a MWL context. Prieto et al.

(2016) singled out two different states of the source, a low and a more active one, and studied them separately.

In this paper, the MAGIC monitoring data set of M 87 between 2012 and 2015 is presented. No major flare is detected in this period, which allows us to study the source in a low-flux state. The data quality is sufficient to constrain some emission models and study the MWL SED of M 87 from radio to VHE gamma-ray frequencies, using MAGIC and available MWL data.

This paper is structured as follows: The observations and data analysis for the several instruments involved are presented in Section 2. The results, consisting of the long-term light curves, skymaps and SEDs of the source in a MWL context are reported and described in detail in Section 3. The SED modelling is discussed in Section 4 and conclusions are summarized in Section 5.

2 OBSERVATIONS AND ANALYSIS

In the following, the data collected within this MWL campaign, ordered from the highest (gamma rays; MAGIC) to lowest energies (radio; VLBA – Very Long Baseline Array), are presented.

2.1 MAGIC

MAGIC is a stereoscopic system of two 17-m-diameter imaging atmospheric Cherenkov telescopes situated at Roque de los Muchachos, Canary Islands, La Palma. An integral sensitivity corresponding to 0.66 ± 0.03 per cent of the Crab Nebula flux above 220 GeV is achieved in 50 h at low zenith angles (see Aleksić et al. 2016, for details on the telescopes performance).

M 87 observations were performed regularly during the visibility period between December and July in the years 2012–2015. The observations took place at zenith angles ranging from $15°$ to $50°$ during dark time and under moonlight conditions. Data were analysed using the standard MAGIC Reconstruction Software (MARS; Zanin et al. 2013). Further details on the stereo MAGIC analysis and on the telescopes' performance under moonlight can be found in Aleksić et al. (2016) and Ahnen et al. (2017), respectively.

2.2 *Fermi*-LAT

The Large Area Telescope (LAT) on board the *Fermi* satellite is a pair-conversion telescope that covers the energy range from 20 MeV to more than 300 GeV, with an angular resolution of $\theta_{68 \text{ per cent}} = 0°.8$ at 1 GeV and a field of view of 2.4 sr (Atwood et al. 2009). The unbinned likelihood analysis of the *Fermi*-LAT data was based on the publicly available Pass 8 photon data set.[1] The data were analysed with the Fermi Science Tools package (version v10r0p5), using the `Source` (P8R2_SOURCE_V6) event class. The M 87 light curve was constructed for $E > 300$ MeV with 30-d time bins. All events within $8°$ of the region of interest centred at the catalogue position of M 87 were selected. A dedicated likelihood analysis was performed on each time bin. All point sources from the LAT source catalogue (3FGL; Acero et al. 2015) that lied within a $12°$ circle from M 87 were included in the model over each time interval. The resulting average flux was found to be $(6.85 \pm 0.56) \times 10^{-9}$ cm^{-2} s^{-1}. *Fermi*-LAT flux densities and the energy spectra were both found to be consistent with the values reported in the 3FGL.

2.3 *Chandra*

The data reduction procedure of the X-ray data set was performed following the Chandra Interactive Analysis of Observations (CIAO) threads,[2] using CIAO version 4.7 and Chandra Calibration Database (CALDB) version 4.6.9. The X-ray images were 'registered' aligning the nuclear X-ray position to the location of the radio core (see for additional details Massaro et al. 2010, 2012, 2013).

To measure observed fluxes for the nuclear emission as well as for any jet feature, a region of size and shape appropriate to the observed X-ray emission was chosen. The background contamination was estimated using two regions with the same shape and size as the science targets but offset from the jet (Massaro et al. 2015).

A 1σ error was calculated based on the square root of the number of counts (the standard deviation of a Poissonian distribution) in the source and background regions. Fluxes reported here were also corrected for the Galactic absorption assuming a photon index of -2 and a value for the Galactic column density of 1.94×10^{-20} cm (Kalberla et al. 2005).

More details on the X-ray data reduction and analysis can be found in Massaro et al. (2009a, b) and Massaro, Harris & Cheung (2011).

2.4 *HST*

HST (*Hubble Space Telescope*) data presented here were obtained with the Space Telescope Imaging Spectrograph (STIS). These imaging data were obtained using the near-ultraviolet (NUV) Multi-Anode Microchannel Array (MAMA) detector of STIS, which has a pixel scale of 0.024 arcsec per pixel providing the best resolution currently available with *HST* (Maclay et al. 2019). The filter in use for these observations was the *F25QTZ* filter, which is a long-pass quartz filter centred at 2360 Å with a full width at half-maximum of about 1000 Å. More details on the sensitivity and throughput of this filter are given in the STIS instrument handbook (Hernandez 2014).

Aperture corrections were applied following Proffitt et al. (2003). In addition, an extinction correction of $A(F25QTZ) = 0.190$ mag (Cardelli, Clayton & Mathis 1989) was applied and fluxes were converted into erg cm^{-2} s^{-1} Å^{-1}.

The *HST*-1 knot located 0.85 arcsec from the center of the galaxy was clearly distinguished from the AGN, as well as other knots 'downstream'. A more detailed account of recent observations of M 87 with the *HST* is given in Madrid (2009) and Perlman et al. (2011).

2.5 Liverpool Telescope

The optical polarization data were taken with the 2-m Liverpool Telescope (LT; Steele et al. 2004) located on the Canary Island of La Palma. The 2012 observations were performed as a part of the Ringo2 blazar programme (Jermak et al. 2016) and 2014–2015 observations using the Ringo3 polarimeter (Arnold et al. 2012). Ringo2 observations were performed using a $V + R$ hybrid filter.

The Ringo3 polarimeter consists of a rotating polaroid (one rotation every 4 s), which captures eight images of the source at successive $45°$ rotations of the polaroid. These eight exposures could be combined according to the equations in Clarke & Neumayer (2002) to determine the degree and angle of polarization. Ringo3 data are separated into three wavelength bands using dichroic mirrors rather than standard filters.

---

[1] http://fermi.gsfc.nasa.gov/cgi-bin/ssc/LAT/LATDataQuery.cgi

[2] http://cxc.harvard.edu/ciao/guides/index.html

A gap between Ringo2 and Ringo3 data in this work was due to the time needed to upgrade of the polarimeter.

2.6 EVN

The **E**uropean **V**ery Long Baseline Interferometer (VLBI) **N**etwork (EVN[3]) is an interferometric array of radio telescopes spread throughout Europe (and beyond). It conducts unique high-resolution radio astronomical observations of cosmic radio sources.

Radio flux densities were taken with EVN during 2012–2015. M 87 was observed with EVN for a total of 10 epochs between 2012 January and 2015 May as a part of the long-term M 87/*HST*-1 monitoring project starting from mid-2009 (Giovannini et al. 2011; Giroletti et al. 2012; Hada et al. 2014, 2015). For all the observations, the data were recorded and correlated at the Joint Institute for VLBI in Europe (JIVE; see Giroletti et al. 2012; Hada et al. 2014, 2015 for some more detailed information). The initial data calibration and fringe-fitting was performed in Astronomical Image Processing System (AIPS[4]) based on the standard VLBI reduction procedures. The final images were produced in the DIFMAP software (Shepherd, Pearson & Taylor 1994) after several cycles of phase and amplitude self-calibration. For the core, the peak flux densities were convolved with a 5/10-milliarcsecond (mas) circular Gaussian beam for 5-GHz/1.7-GHz data, respectively.

2.7 VERA

Between 2011 September and 2012 September, the core of M 87 was densely monitored with the VLBI Exploration of Radio Astrometry (VERA), a Japanese VLBI network consisting of four stations operated at 22 and 43 GHz. A total of 24 epochs were obtained at 22 GHz throughout the period, and additional five sessions were performed at 43 GHz between 2012 February and May. Detailed descriptions of the data analysis as well as some images were presented in Hada et al. (2014). In this paper, an improved amplitude calibration procedure was applied to better take into account the amplitude loss due to multiple signal digitization processes during data recording (Iguchi et al. 2005). Peak flux densities of the M 87 core (at 22 and 43 GHz) were provided, which were measured with a common 0.6-mas-diameter circular Gaussian convolving beam. An amplitude uncertainty of 10 per cent for each data set was assumed.

2.8 VLBA

During the period discussed in this paper, five high-resolution radio observations of M 87 were made at 43 GHz using the VLBA (Napier et al. 1994). Those observations were designed to monitor the ambient structure of M 87 in support of observations, which would have been made in response to a flare in the gamma-ray energy band. No such flare occurred. A major upgrade to the VLBA digitization and recording hardware was occurring during this period,[5] which provided an improvement in sensitivity by a factor of 2. Changes also occurred in the flux-density calibration methods and standards used (Walker 2014). The data were processed in AIPS using standard methods. Additional details about the reduction of the VLBA data, along with the imaging and analysis results, could be found in Walker et al. (2018).

Table 1. Effective observation time and significance of the VHE gamma-ray signal observed from M 87 above 300 GeV between 2012 and 2015.

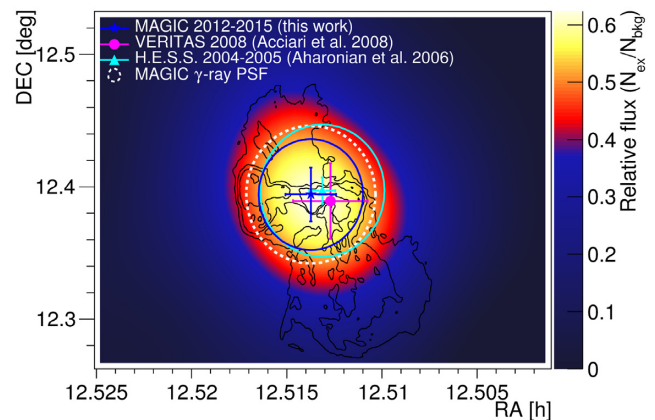| Year	T_{eff} (h)	Significance$_{E > 300\,GeV}$ (σ)
2012	38.75	5.41
2013	34.82	8.75
2014	49.88	7.29
2015	32.72	5.96

Figure 1. Averaged VHE gamma-ray sky map above 300 GeV of M 87 derived from 2012–2015 MAGIC stereo observations centred on the position of the VHE gamma-ray emission obtained from a two-dimensional Gaussian fit (blue star). The PSF (white dashed circle) of the MAGIC telescopes for a gamma-ray signal is shown. The positions fitted to the VHE gamma-ray signal observed by MAGIC from 2012 to 2015 (blue star), by H.E.S.S. from 2004 to 2005 (light blue triangle; Aharonian et al. 2006), and by VERITAS in 2007 (magenta point; Acciari et al. 2008) are shown. The circles (solid blue and light blue lines) indicate the 99.9 per cent confidence-level upper limit of an extended gamma-ray signal from MAGIC and H.E.S.S. observations, respectively. The VLA radio image (black contours) at 327 MHz (Owen et al. 2000) is shown as a reference.

3 RESULTS

In the following, the results of this MWL campaign are presented, starting with the detection in the TeV band by MAGIC in Section 3.1, followed by the discussion on the MWL light curves in Section 3.2, and concluding with the characterization of the SED in the GeV–TeV band in Section 3.3.

3.1 Detection and sky maps with MAGIC

MAGIC has detected M 87 in every yearly campaign between 2012 and 2015. Table 1 lists the effective observation time and significance of the VHE gamma-ray signal. The significance of the detection is calculated according to equation (17) in Li & Ma (1983). In Fig. 1, the contours of the radio image taken with Very Large Array (VLA) at 327 MHz (Owen et al. 2000) are superimposed on the VHE gamma-ray relative-flux sky map, showing the corresponding point spread function (PSF) of the MAGIC telescopes (0°.052) and the upper limit at 99.9 per cent confidence level of an extended VHE gamma-ray signal, which is of the size of 0°.042, corresponding to 11.5 kpc. An enhanced point-like gamma-ray signal is found at the position of the catalogue position of M 87. The locations of the VHE gamma-ray emission observed by H.E.S.S. (Aharonian et al. 2006) and VERITAS (Acciari et al. 2008) are indicated in Fig. 1 as well.

Table 2. Mean integral flux above 300 GeV observed with MAGIC between 2012 and 2015 obtained from a fit with a constant to the ∼20-d binned light curves.

Year	$F_{>300\,\mathrm{GeV}}$ (10^{-12} cm^{-2} s^{-1})
2012	1.18 ± 0.25
2013	1.72 ± 0.30
2014	1.49 ± 0.22
2015	1.25 ± 0.33
2012-2015	1.44 ± 0.13

3.2 Multiwavelength light curves

The variability of the VHE gamma-ray flux is investigated at different time-scales. The mean integral flux of each year, which is obtained by a fit with a constant, is reported in Table 2. No variability is observed across the data set, the only exception being a hint of variability on a daily scale observed in 2013 (the probability for a constant flux is 0.3 per cent). For the other years, the light curves are found to be compatible with a constant flux with a probability higher than 38 per cent. Assuming an additional systematic uncertainty of 11 per cent of the measured flux (Aleksić et al. 2016) for the 2013 data, a probability for a constant flux of 0.9 per cent is obtained.

To compare the new data collected between 2012 and 2015 with previous M 87 observations, the integral flux is calculated for 400 GeV < E < 1 TeV and compared with previous MAGIC, H.E.S.S., and VERITAS observations (Aharonian et al. 2006; Acciari et al. 2008; Albert et al. 2008; Aleksić et al. 2012; Aliu et al. 2012); see Table 3. The integral flux level between 2012 and 2015 is
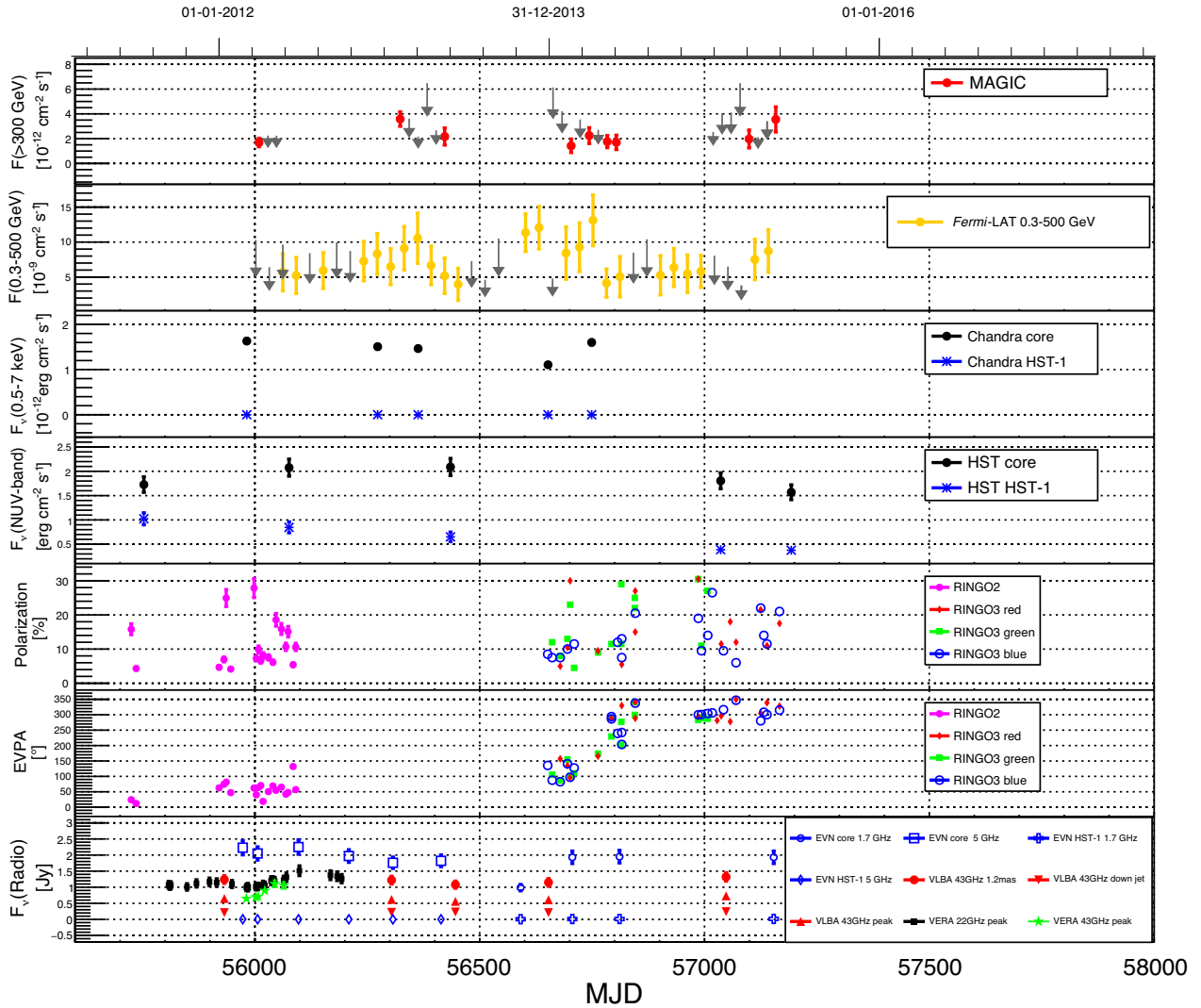

Figure 2. MWL light curve between 2012 and 2015: From top to bottom: VHE and HE gamma-ray data by MAGIC and *Fermi*-LAT, respectively. Upper limits at the 95 per cent confidence level are indicated by downward grey arrows (see text for details). The *Chandra* X-ray fluxes from the core (points) and *HST*-1 (asterisks) are shown in the third panel from the top. The X-ray observations are corrected for Galactic absorption (see text for details). In the fourth panel from the top, the NUV data are presented from the core as full points and from *HST*-1 as stars. NUV data have been corrected for interstellar extinction following Cardelli et al. (1989). Optical polarization data taken with the V + R filter by the LT with Ringo2 in 2012 (filled circles) and with Ringo3 in 2014–2015 (empty circles, filled squares, and diamonds for blue, green, and red bands, respectively) are shown in the dedicated panels. The bottom panel presents radio data provided by the EVN (blue open symbols), VLBA (red filled symbols), and VERA (black empty and filled stars). The light curves are daily binned except VHE and HE gamma rays, where roughly 20- and 30-d binning is applied, respectively.

Table 3. Comparison of the integral fluxes (400 GeV < E < 1 TeV), spectral indices, and differential fluxes observed in 2004-2005 with H.E.S.S. (Aharonian et al. [2006]), 2005–2007 with MAGIC (Aleksić et al. [2012]), in 2007 and 2010 with VERITAS (Acciari et al. [2008]; Aliu et al. [2012]), in 2008 with MAGIC (Albert et al. [2008]), and between 2012 and 2015 with MAGIC (this work). The integral fluxes are extrapolated from the simple power-law fits to the observed spectra. The differential flux is compared for the decorrelation energy of 784 GeV obtained for the data of this work, adopting the parameters of the individual fits. The values shown include only statistical errors and are obtained by error propagation assuming the errors of the flux normalization and the spectral index to be uncorrelated.

Array	Year	$F_{400\,\mathrm{GeV}<E<1\,\mathrm{TeV}}$ (10^{-12} cm^{-2} s^{-1})	Γ	$f_{E=784\,\mathrm{GeV}}$ (10^{-12} TeV^{-1} cm^{-2} s^{-1})
H.E.S.S.	2004	0.51 ± 0.22	-2.62 ± 0.35	0.46 ± 0.15
H.E.S.S.	2005	1.97 ± 0.44	-2.22 ± 0.15	2.01 ± 0.28
MAGIC	2005$-$2007	0.90 ± 0.44	-2.21 ± 0.21	0.92 ± 0.24
VERITAS	2007	1.31 ± 0.38	-2.31 ± 0.17	1.30 ± 0.23
MAGIC	2008	5.09 ± 1.00	-2.30 ± 0.11	5.06 ± 0.66
VERITAS	2010	7.82 ± 0.80	-2.19 ± 0.07	8.03 ± 0.51
MAGIC	2012$-$2015	0.74 ± 0.08	-2.41 ± 0.07	0.71 ± 0.06

Table 4. Probability of a constant flux observed in the individual wavebands (see Fig. 2).

Waveband	Constant flux probability	χ^2/d.o.f.
HE	1.8×10^{-22}	192/38
X-rays (core)	7.5×10^{-15}	72.29/4
X-rays (*HST*-1)	6.5×10^{-10}	48.87/4
UV (core)	0.11	7.64/4
UV (*HST*-1)	1.4×10^{-6}	32.63/4
Radio		
VLBA$^{\bullet}$ (1.2 mas)	0.67	2.37/4
VLBA$^{\blacktriangle}$ (Peak)	0.44	3.73/4
VLBA$^{\blacktriangledown}$ (down jet)	0.88	1.22/4
EVN$^{\square}$ (core)	0.40	5.15/5
EVN$^{\circ}$ (core)	1.1×10^{-8}	39.95/3
EVN$^{\diamond}$ (*HST*-1)	1.5×10^{-13}	69.27/5
EVN$^{\triangle}$ (*HST*-1)	0.12	5.85/5
VERA$^{\blacksquare}$ (peak)	1.95×10^{-273}	1360/23
VERA* (peak)	5.90×10^{-60}	287.1/5

Note. $\bullet$, $\blacktriangle$, $\blacktriangledown$: VLBA data at 43 GHz; $\square$, $\diamond$: EVN data at 5 GHz; $\circ$, $\triangle$: EVN data at 1.7 GHz; $\blacksquare$, $\star$: VERA data at 22 and 43 GHz.

compatible with those observed with H.E.S.S. in 2004 (Aharonian et al. [2006]) and with MAGIC between 2005 and 2007 (Aleksić et al. [2012]), when the source was in a low-emission state in the TeV band, which can be defined as some 5–10 per cent of the Crab Nebula flux at energies 400 GeV < E < 1 TeV. The low-emission state is clearly separated from the flaring periods in 2005, 2008, and 2010 (Acciari et al. [2009]; Abramowski et al. [2012]; Beilicke & VERITAS Collaboration [2012]).

The MWL light curve of M 87 between 2012 and 2015 is shown in Fig. 2. Both the core and the innermost knot *HST*-1 in the jet are found to be in a low-emission state. Table 4 shows the constant flux probability and χ^2/d.o.f. from HE to radio data. At lower frequencies, variability is observed for *HST*, *Chandra*, EVN 1.7-GHz core, and 5-GHz *HST*-1 data, as well as VERA peak data at 22 and 44 GHz. No clear variability is found for the EVN 1.7-GHz *HST*-1 and 5-GHz core data, VLBA core and jet data, as well as for the HE (100 MeV < E < 100 GeV) gamma-ray data.

The optical polarimetry data suggest a long-term rotation of the electric vector polarization angle (EVPA) from $\sim$0$°$ to $\sim$400$°$, while the polarization stays in general at the rather low level of less than 5 per cent, except some higher polarization of up to $\sim$25 per cent around the beginning of the MAGIC observation period in 2012. Since the EVPA in blazars depends on the orientation of the shocks

and the magnetic field threading it, EVPA provides an important tool to understand the acceleration mechanism of the shocked plasma. In recent studies, EVPA swings larger than 180$°$ simultaneous to gamma-ray emission have been interpreted as additional evidence for a helical structure of the magnetic field (Marscher et al. [2010]; Abdo et al. [2010]; MAGIC Collaboration [2018]). However, in the present case, the EVPA rotation happens over several weeks (approximately from MJD 56704 to MJD 56824 – 2014 February 16 to June 16), making it difficult to find a connection to the activity in the other bands. EVPA rotations can be due to the reconnection in the emission region of the jet during a high-activity state. However, no flare has been observed in the present data sample to be associated with a reconnection event.

3.3 SED in the TeV band

The VHE gamma-ray SED observed with MAGIC is well described[6] by a power law of the form $E^2 \mathrm{d}N/\mathrm{d}E = f_{\mathrm{0VHE}}(E/E_{\mathrm{0VHE}})^{\Gamma_{\mathrm{VHE}}+2}$, with the flux normalization f_{0VHE} being $(4.31 \pm 0.33) \times 10^{-13}$ cm^{-2} s^{-1} TeV^{-1}, at a decorrelation energy[7] E_{0VHE} of 784 GeV and a spectral index Γ_{VHE} equal to -2.41 ± 0.07. The errors quoted here are only statistical. The observed spectrum is not significantly affected by the extragalactic background light (EBL) absorption due to the proximity of M 87; for this source, the production of electron–positron pairs by interaction with the EBL becomes significant at higher energies, above 10 TeV (Neronov & Aharonian [2007]). The spectral indices and differential fluxes at the decorrelation energy from previous VHE gamma-ray observations are reported in Table 3. All spectral indices observed during both high- and low-emission states are mostly compatible within the statistical errors. The differential flux between 2012 and 2015 is on a similar level as during the low-emission states reported by MAGIC between 2005 and 2007, and by H.E.S.S. in 2004, whereas it is lower with respect to the flux level observed during the flaring states in 2005, 2008, and 2010.

The averaged VHE–HE gamma-ray SED between 2012 and 2015 is shown in Fig. 3. A simple power law (red line in Fig. 3) is fitted to the combined VHE–HE gamma-ray SED, yielding a spectral index and a flux normalization of $\Gamma = -2.24 \pm 0.01$

---

[6] χ^2/d.o.f. = 3.87/3, corresponding to a fit probability of 28 per cent.
[7] The decorrelation energy corresponds to the energy at which the correlation between the flux normalization and spectral index is minimum.
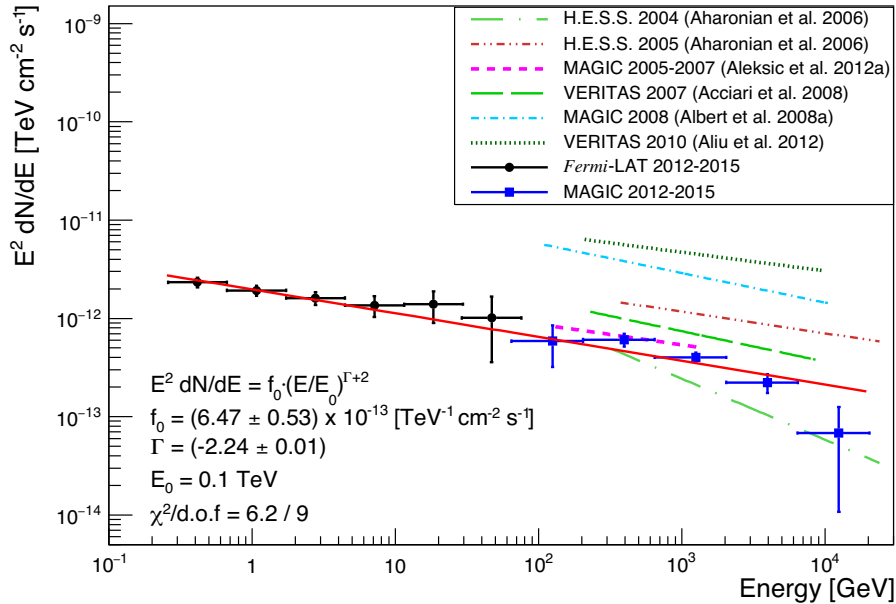
Figure 3. Combined MAGIC (blue filled squares) and quasi-simultaneous *Fermi*-LAT (black filled circles) SED between 2012 and 2015, to which a simple power law (solid red line) is fitted. For comparison, the simple power-law fits describing the averaged SEDs of the low-emission states observed in 2004 with H.E.S.S. (green long-dash–dotted line; Aharonian et al. 2006) and 2005–2007 with MAGIC (magenta dashed line; Aleksić et al. 2012), and of the flaring state observed in 2005 with H.E.S.S. (red short dash–dotted line; Aharonian et al. 2006), in 2007 and 2010 with VERITAS (green long-dashed and dotted lines; Acciari et al. 2008; Aliu et al. 2012), and in 2008 with MAGIC (blue short-dash–dotted line; Albert et al. 2008) are shown.

and $f_{0(E=100\,\mathrm{GeV})} = (6.47 \pm 0.53) \times 10^{-13}\,\mathrm{cm^{-2}\,s^{-1}\,TeV^{-1}}$, respectively, at normalization energy $E_0 = 100\,\mathrm{GeV}$. While *Fermi*-LAT data are collected throughout the four years, MAGIC data for reasons of visibility of the source are taken each year during the December–July time window.

4 SED MODELLING

In Tavecchio & Ghisellini (2008), a structured-jet model (Ghisellini et al. 2005) is applied, assuming a jet with a fast spine and a slower layer and, thus, two zones to explain the TeV flares. Aleksić et al. (2012) apply this scenario to model the low-state SED in 2005–2007. Lenain et al. (2008) propose that the flaring emission would occur while the jet is collimating, and Georganopoulos et al. (2005) while it is decelerating. An alternative process to explain these VHE gamma-ray flares was proposed by Giannios et al. (2010), which is based on misaligned mini-jets driven by magnetic reconnection moving within the jet at relativistic velocities. Istomin & Sol (2009) propose a two-step acceleration model to TeV energies involving initial particle acceleration within the accretion disc and then, further, centrifugal acceleration in the rotating magnetosphere. Levinson & Rieger (2011) discuss the variable TeV emission to be possibly produced in a starved magnetospheric region.

Despite the long-term investment in M 87 monitoring, the production site of TeV gamma rays remains unclear, with strong hints, however, that it will be close to the core of the jet (some 40–100R_S from the black hole), suggested by the correlation with radio and X-ray activities (Acciari et al. 2008). *HST*-1 has also been discussed as a possible production site of the TeV emission because of a rapid TeV flare in 2006 (Harris et al. 2006), which coincides with an enhanced X-ray flux of this knot, while no enhanced flux from the nucleus is observed. However, the association with *HST*-1 seems unlikely given the absence of radio or X-ray short-time-scale

variabilities detected from this region, whereas several occasions of gamma-ray variability on daily time-scales were seen. Another caveat to this interpretation is given by the fact that VLBA data have shown the compact knots in *HST*-1 to be essentially unresolved, approaching the size limits set by the TeV-emission variability, as reported in Cheung, Harris & Stawarz (2007).

In this paper, the question whether a self-consistent modelling of a single emission region can explain the observed data in the low-flux state and what consequences such scenario would have is investigated. Fig. 4 shows the MWL SED of the radio core of M 87. To build the SED, quasi-simultaneous data are used, taken between 2012 and 2015 from MAGIC, *Fermi*-LAT, *Chandra*, *HST*, EVN at 1.7 GHz and 5 GHz, and VLBA at 43 GHz. NUV data are corrected for interstellar extinction following Cardelli et al. (1989). No averaging is performed for the low-energy data from radio to X-ray, where variability has been observed.

As no clear variability in the TeV regime is detected, the model constraints are relaxed with respect to those for flaring states. The acceleration and emission zones are assumed to be directly connected, representing the downstream region of a shock front. Additionally, the relevant parts in the quasi-simultaneous MWL data connected to the TeV gamma-ray emitting zone are assumed to be the HE gamma-ray data from *Fermi*-LAT and the X-ray data detected for the core region by *Chandra*. In general, radio emission tends to have a spatially extended emission region, and can be subject to synchrotron self-absorption in the core region due to a high magnetic field strength leading to a high opacity in this band. However, usually this absorption effect is more severe for hadronic models than it is for leptonic scenarios, where a less strong magnetic field is required. We therefore assume the radio emission observed by VLBA and EVN originates from a larger region. The NUV data from *HST* detected for the core of M 87 presumably have origin from a region much closer to the black hole and where the jet is launched, as suggested by general relativistic radiation
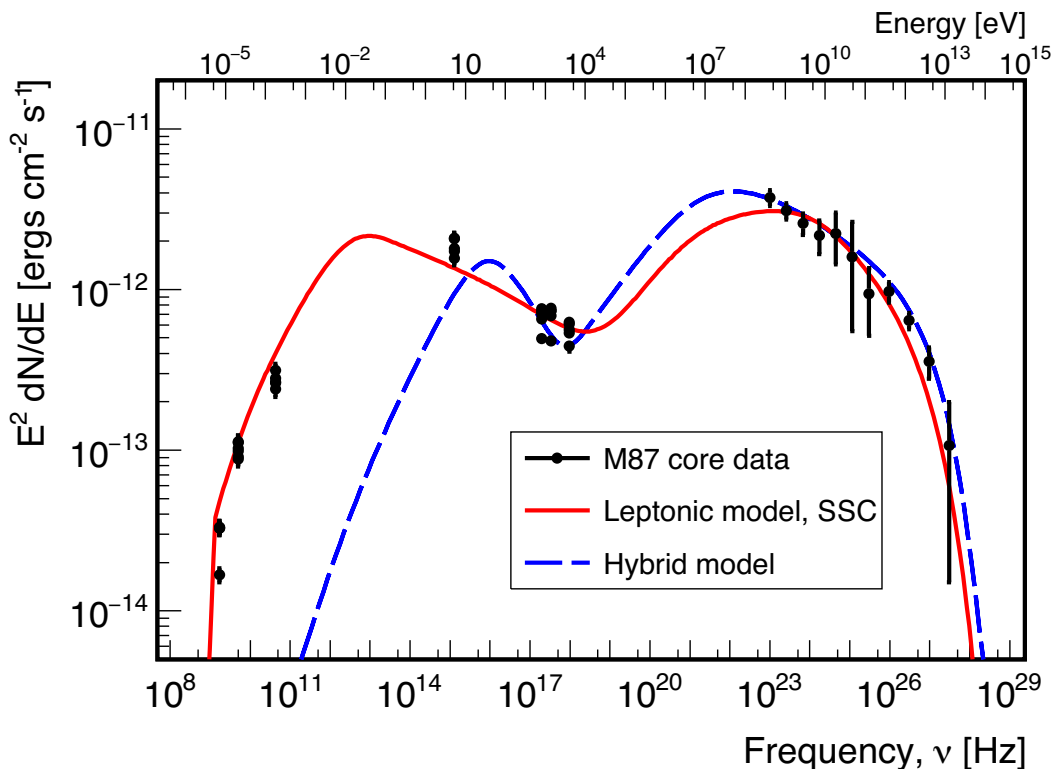
Figure 4. MWL SED of the radio core of M 87 compiled from quasi-simultaneous 2012–2015 observations (black points). VHE gamma-ray observations by MAGIC are combined with HE gamma-ray data from *Fermi*-LAT, X-ray data from *Chandra*, NUV data from *HST*, radio data at 1.7 GHz and 5 GHz provided by EVN, and at 43 GHz by VLBA. The models represent two possible scenarios: In the leptonic scenario (red solid line), the HE component is dominated by the synchrotron self-Compton (SSC) emission, whereas in the hybrid scenario (blue dashed line), the HE emission is dominated by the synchrotron radiation of relativistic protons.

magnetohydrodynamics (see, e.g. Ryan, Dolence & Gammie 2015). Therefore, we concentrate on the X-ray, GeV, and TeV data rather than the radio-to-optical data for our modelling.

First, the leptonic model is applied to account for the broadband spectrum of M 87 with the numerical code in Asano et al. 2014, neglecting Fermi-II acceleration (see also Asano & Hayashida 2015, 2018). The code calculates the temporal evolution of the electron and photon energy distributions in the plasma rest frame along the jet (at radius R from the black hole), which is similar to the `blazar` code in Moderski, Sikora & Błażejowski 2003 (for application examples, see, e.g. Kataoka et al. 2008; Hayashida et al. 2012). Here, a steady conical outflow is assumed, in which the temporal evolution along the jet is equivalent to the radial evolution. The conically expanding jet naturally leads to the adiabatic cooling of electrons, which is a similar effect to the electron escape in one-zone steady models. In this one-dimensional (1D) code, the parameter for the electron escape is not required. The magnetic field decreases as $B = B_0(R/R_0)^{-1}$. The macroscopic model parameters are the Lorentz factor Γ_L, the initial radius R_0 (distance from the black hole), the initial magnetic field B_0, the electron luminosity L_e (including the counter jet), the jet opening angle θ_j, and the viewing angle θ_v. Here, $\Gamma_L = 3$, $\theta_j = 1/\Gamma_L = 19°$, and $\theta_v = 15°$, and half-opening angle of the jet are adopted (Biretta et al. 1999; Acciari et al. 2009; Walker et al. 2018), where the half-opening angle is well below the average apparent full-opening angle inferred from radio observations (Walker et al. 2018). Electrons are injected during the dynamical time-scale $R_0/(c\Gamma_L)$ in the plasma rest frame. In this time-scale, the injection rate into a given volume $V \propto R^2$

is constant. The evolutions of the electron energy distribution and photon emission are calculated as far as $R = 30R_0$, taking into account synchrotron emission and inverse Compton scattering with the Klein–Nishina effect, gamma–gamma absorption, secondary pair injection, synchrotron self-absorption, and adiabatic cooling. The model parameters for the electron injection spectrum are the minimum and maximum electron Lorentz factors ($\gamma_{\min}$ and $\gamma_{\max}$), the location of the break in the electron energy distribution (γ_{br}), and power-law indices p_1 and p_2 for below and above γ_{br}, respectively. The parameter values are summarized in Table 5.

Secondly, a hybrid model is applied assuming that protons and electrons are accelerated in the jet. The fully time-dependent implementation is based on the geometry of Weidinger & Spanier (2010). The acceleration mechanism and the implementation of all leptonic processes are adopted from Richter & Spanier (2016), and the photohadronic framework is implemented following Hümmer et al. (2010). The acceleration of particles is closely modelled to the Fermi-I acceleration. Under the assumption that the particle distribution is quickly reaching isotropy in the downstream region of the shock, the model follows the evolution of the injected, monoenergetic particle distribution towards a power law. The shape of the particle distribution and the relevant time-scales follow consistently from the input shock parameters.

The simulated SED, computed with the hybrid model that best describes the observed broad-band SED, is shown in Fig. 4 (blue dashed line) together with the available quasi-simultaneous data. It is not clear whether a unique set of parameters exists for describing the SED, and the high dimensionality of the parameter space does

Table 5. Parameters used for the models shown in Fig. 4. Parameters of the Leptonic model are described in the text. Parameters of the hybrid model are explained in Table 6.

Leptonic	Γ_L	R_0 $(10^{17}\,\mathrm{cm})$	B_0 (mG)	L_e $[10^{44}\,\mathrm{erg\,s^{-1}}]$	θ_j (°)	θ_v (°)	γ_{min}	γ_{br}	γ_{max}	p_1	p_2
	3	4.0	3.1	2.4	19	15	500	1.4×10^4	3.0×10^7	1.9	3.2

Hybrid	R_{acc} $(10^{12}\,\mathrm{cm})$	R_{rad} $(10^{15}\,\mathrm{cm})$	N_{inj}^{p} $(10^{42}\,\mathrm{cm\,s^{-1}})$	γ_{inj}^{p}	N_{inj}^{e} $(10^{40}\,\mathrm{cm\,s^{-1}})$	γ_{inj}^{e} (10^3)	B (G)	r	η_e	$\mathcal{D}$
	35	30	8.77	10	2	10	3	3.50	1	5.3

Table 6. Description of the parameters used in the hybrid modelling of the broad-band SED.

R_{rad}	Size of the radiation zone
R_{acc}	Size of the acceleration zone
$\gamma_{inj}^{species}$	Energy injected
B	Magnetic field strength
η	Particle diffusion coefficient
V_S	Shock speed
r	Shock compression ratio
$\mathcal{D}$	Doppler factor

not allow for χ^2 fitting. The community standard is therefore to optimize the SED modelling by manual parameter changes until data points, and especially slopes, are agreeing with the observed SED. In the hybrid model, the radio-to-X-ray radiations originate from the synchrotron emission of electrons. The emission at HE, due to the high magnetic field and the assumption of protons being injected into the acceleration zone, is dominated by the synchrotron emission of protons in this case. The parameters used for the presented fit are summarized in Table 5, and the most important parameters of the model are described in Table 6. The shock speed is set to $V_S = 0.1c$ and Fermi-II acceleration is neglected. The spatial diffusion coefficient η is mass-dependent, and we will use $\eta_e = \eta$ as a reference value and calculate the proton coefficient as $\eta_p = m_p/m_e\eta$. The escape time from each region is calculated as $t_{esc} = \eta R/c$ and the acceleration time-scale follows, depending on the spectral index, from $t_{acc} = \eta R_{acc}/c \gtrsim t_{esc}$ (for further reading, see, e.g. Protheroe & Clay 2004). It has to be noted that *Chandra* data are in the sensitive area of the transition between the two bumps (10^{17}–10^{18} Hz) in the hybrid model. In addition, the number of parameters is higher than in the leptonic model and the two components (self-Compton from electrons and synchrotron from protons) are basically independent of each other, as their densities are assumed to be uncorrelated. The hybrid model covers electrons and protons simultaneously. Hence, self-Compton and proton synchrotron emission exists within the same model.

The MAGIC observations reveal that the GeV–TeV emission is compatible with a single emission component, either self-Compton from the leptons or synchrotron from protons. The component from radio to X-rays is also explained by the synchrotron component of leptons in both scenarios. However, in the leptonic scenario, radio and X-rays would originate from the same region as the GeV–TeV data, whereas in the hybrid scenario they would come from a different and a much larger region. The required electron luminosity ($L_e = 2.4 \times 10^{44}\,\mathrm{erg\,s^{-1}}$ including the counter jet) is comparable to the total jet power estimated from the large-scale radio structure (Owen et al. 2000). However, the relatively high SSC flux requires a very low magnetization: The energy–density ratio of the magnetic field to the non-thermal electrons is 5.2×10^{-5} at $R = 2R_0$, which

is much smaller than the values found in other blazars (10^{-1}–10^{-2}, Asano & Hayashida 2018).

Asada & Nakamura (2012) claim that the radio image of the M 87 jet is consistent with a parabolic streamline, also confirmed by Hada et al. (2013), which supports the magnetically driven jet model (Komissarov et al. 2009). Later, Asada et al. (2014) show that the gradual acceleration through a distance of 10^6 times the Schwarzschild radius also supports the magnetically driven jet model. In addition Kino et al. (2015) point out that the radio data at 230 GHz obtained by the Event Horizon Telescope (EHT) imply a magnetically dominated jet. Those results seem inconsistent with the very low magnetization at ∼200 times the Schwarzschild radius indicated by the broad-band SED. Other than the large-scale component constrained by radio observations, a very low magnetized emission region is required to explain the gamma-ray spectrum by the leptonic model. Such a very low jet magnetization in the emitting region (the energy in leptons is five orders of magnitude higher than the energy in the magnetic field) is very far from the equipartition scenario. This suggests an emission region far from the core of the jet or a very efficient mechanism to convert Poynting flux into a matter-dominated jet.

A similar low magnetization in the leptonic modelling of blazars is also reported in Tavecchio & Ghisellini (2016), where the sample of BL Lacs used for the study was characterized by a small value of the magnetic energy density and a relatively large Doppler factor, not easy to be explained in a one-zone SSC scenario, but justified in a spine-layer model, supporting the hypothesis of structured jets in BL Lac objects.

New results from the EHT (Event Horizon Telescope Collaboration 2019a) favour the hypothesis of the accretion disc as the origin of the observed emission at 230 GHz. However, given the fact that many of the used models produce images consistent with the EHT data, they suggest that the image shape is mainly controlled by gravitational lensing and the space–time geometry, rather than details of the plasma physics.

The physical picture of the M 87 jet remains unrevealed yet, which provides great motivation for future observational and theoretical study of this object and blazars in general.

5 CONCLUSIONS

MAGIC has monitored M 87 from 2012 to 2015 for a total of 156 h after quality cuts. The source is detected at a low state in every yearly campaign between 2012 and 2015. No clear variability is observed in the 2012, 2014, and 2015 data on daily and ∼20-d time-scales. A hint of variability (∼ 3σ level) is found in 2013 data on a daily time-scale, remaining at a similar significance level even when variable systematic uncertainties of the MAGIC measurements are taken into account. The VHE gamma-ray flux level above 300 GeV between 2012 and 2015 is the lowest flux observed since 2005.

No clear variability was found at lower frequencies for the VLBA core and the jet data, nor for the EVN 1.7 and 5-GHz data for *HST*-1 and the core, respectively. However, variability was observed in *HST*, *Chandra*, EVN 1.7-GHz core and EVN 5-GHz *HST*-1 data, and VERA peak data at 22 and 44 GHz. The optical polarimetry data suggest a long-term rotation from ∼0° to ∼400°. The polarization stays in general at a rather low level, below 5 per cent, except some higher polarization of up to ∼ 25 per cent around the beginning of the MAGIC observation period in 2012.

The energy spectrum of M 87 is found to have the same shape (within the statistical uncertainties) during the observations presented here and during the TeV flares observed in the past. Remarkably, the combination with *Fermi*-LAT data at GeV energies reveals a continuous photon spectrum over five orders of magnitude in energy, which is consistent with a simple power law.

The broad-band SED is found to be consistent with leptonic and hybrid emission scenarios where the GeV–TeV component corresponds to the self-Compton or synchrotron radiation from leptons and hadrons, respectively. An important result from the leptonic modelling is that the required jet magnetization in the emitting region is very low (the energy in leptons is five orders of magnitude higher than that in the magnetic field) and, thus, very far from the equipartition scenario. This implies either an emission region far from the core of the jet or a very efficient mechanism to convert Poynting flux into a matter-dominated jet.

Both leptonic and hybrid models provide a good description of the data. However, the hybrid scenario is more consistent with the HE and VHE gamma-ray part of the SED. For this reason, it is preferred in describing the present low state of the source..

Further dense and precision MWL observations of M 87 are necessary to unveil the nature of the emission and its spatial location.

ACKNOWLEDGEMENTS

REFERENCES

Abdo A. A. et al., 2010, Nature, 463, 919
Abramowski A. et al., 2012, ApJ, 746, 151
Acciari V. A. et al., 2008, ApJ, 679, 397
Acciari V. A. et al., 2009, Science, 325, 444
Acciari V. A. et al., 2010, ApJ, 716, 819
Acero F. et al., 2015, ApJS, 218, 23
Aharonian F. et al., 2003, A&A, 403, L1
Aharonian F. et al., 2006, Science, 314, 1424
Ahnen M. L. et al., 2017, Astropart. Phys., 94, 29
Albert J. et al., 2008, ApJ, 685, L23
Aleksić J. et al., 2012, A&A, 544, A142
Aleksić J. et al., 2016, Astropart. Phys., 72, 76
Aliu E. et al., 2012, ApJ, 746, 141
Arnold D. M., Steele I. A., Bates S. D., Mottram C. J., Smith R. J., 2012, in McLeanI. S., Ramsay S. K., Takami H., eds, Proc. SPIE Conf. Ser. Vol. 8446, in Ground-Based and Airborne Instrumentation for Astronomy IV. SPIE, Bellingham , p. 84462J
Asada K., Nakamura M., 2012, ApJ, 745, L28
Asano K., Hayashida M., 2015, ApJ, 808, L18
Asano K., Hayashida M., 2018, ApJ, 861, 31
Asada K., Nakamura M., Doi A., Nagai H., Inoue M., 2014, ApJ, 781, L2
Asano K., Takahara F., Kusunose M., Toma K., Kakuwa J., 2014, ApJ, 780, 64
Atwood W. B. et al., 2009, ApJ, 697, 1071
Beilicke M., VERITAS Collaboration, 2012, in Aharonian F. A., Hofmann W., Rieger F. M., eds, AIP Conf. Proc. Vol. 1505, in 5th International Meeting on High Energy Gamma-Ray Astronomy. Am. Inst. Phys., New York, p. 586
Bird S., Harris W. E., Blakeslee J. P., Flynn C., 2010, A&A, 524, A71
Biretta J. A., Sparks W. B., Macchetto F., 1999, ApJ, 520, 621
Cardelli J. A., Clayton G. C., Mathis J. S., 1989, ApJ, 345, 245
Cheung C. C., Harris D. E., Stawarz Ł., 2007, ApJ, 663, L65
Clarke D., Neumayer D., 2002, A&A, 383, 360
De Jong S., Beckmann V., Soldi S., Tramacere A., Gros A., 2015, MNRAS, 450, 4333
Event Horizon Telescope Collaboration, 2019a, ApJ, 875, L5
Event Horizon Telescope Collaboration, 2019b, ApJ, 875, L6
Fanaroff B. L., Riley J. M., 1974, MNRAS, 167, 31 P

Gebhardt K., Adams J., Richstone D., Lauer T. R., Faber S. M., Gültekin K., Murphy J., Tremaine S., 2011, ApJ, 729, 119

Georganopoulos M., Perlman E. S., Kazanas D., 2005, ApJ, 634, L33

Ghisellini G., Tavecchio F., Chiaberge M., 2005, A&A, 432, 401

Giannios D., Uzdensky D. A., Begelman M. C., 2010, MNRAS, 402, 1649

Giovannini G., Casadio C., Giroletti M., Beilicke M., Cesarini A., Krawczynski H., 2011, in Romero G. E., Sunyaev R. A., Belloni T., eds, Proc. IAU Symp. 275, Jets at All Scales. Kluwer, Dordrecht, p. 150

Giroletti M. et al., 2012, A&A, 538, L10

Hada K. et al., 2013, ApJ, 775, 70

Hada K. et al., 2014, ApJ, 788, 165

Hada K. et al., 2015, preprint (arXiv:1504.01808)

Harris D. E., Biretta J. A., Junor W., Perlman E. S., Sparks W. B., Wilson A. S., 2003, ApJ, 586, L41

Harris D. E., Cheung C. C., Biretta J. A., Sparks W. B., Junor W., Perlman E. S., Wilson A. S., 2006, ApJ, 640, 211

Harris D. E., Cheung C. C., Stawarz Ł., Biretta J. A., Perlman E. S., 2009, ApJ, 699, 305

Hayashida M. et al., 2012, ApJ, 754, 114

Hernandez S. et al., 2014, Space Telescope Imaging Spectrograph Instrument Handbook Version 13.0. STScI, Baltimore, MA

Hümmer S., Rüger M., Spanier F., Winter W., 2010, ApJ, 721, 630

Iguchi S., Kkurayama T., Kawaguchi N., Kawakami K., 2005, PASJ, 57, 259

Istomin Y. N., Sol H., 2009, Ap&SS, 321, 57

Jermak H. et al., 2016, MNRAS, 462, 4267

Kalberla P. M. W., Burton W. B., Hartmann D., Arnal E. M., Bajaja E., Morras R., Pöppel W. G. L., 2005, A&A, 440, 775

Kataoka J. et al., 2008, ApJ, 672, 787

Kim Y.-Q., Krichbaum T. P., Lu R.-S., 2018a, A&A, 616, A188

Kim Y.-Q., Lee S.-S., Hodgson J. A., 2018b, A&A, 610, L5

Kino M., Takahara F., Hada K., Akiyama K., Nagai H., Sohn B. W., 2015, ApJ, 803, 30

Komissarov S. S., Vlahakis N., Königl A., Barkov M. V., 2009, MNRAS, 394, 1182

Lenain J. P., Boisson C., Sol H., Katarzyński K., 2008, A&A, 478, 111

Levinson A., Rieger F., 2011, ApJ, 730, 123

Li T. P., Ma Y. Q., 1983, ApJ, 272, 317

Maclay M. et al., 2019, American Astronomical Society Meeting Abstracts, #233. AAS, Seattle WA, p. 157.06

Madrid J. P., 2009, AJ, 137, 3864

MAGIC Collaboration, 2018, A&A, 619, A45

Marscher A. P. et al., 2010, ApJ, 710, L126

Marshall H. L., Miller B. P., Davis D. S., Perlman E. S., Wise M., Canizares C. R., Harris D. E., 2002, ApJ, 564, 683

Massaro F. et al., 2009a, ApJ, 692, L123

Massaro F., Harris D. E., Chiaberge M., Grandi P., Macchetto F. D., Baum S. A., O'Dea C. P., Capetti A., 2009b, ApJ, 696, 980

Massaro F. et al., 2010, ApJ, 714, 589

Massaro F., Harris D. E., Cheung C. C., 2011, ApJS, 197, 24

Massaro F. et al., 2012, ApJS, 203, 31

Massaro F., Harris D. E., Tremblay G. R., Liuzzo E., Bonafede A., Paggi A., 2013, ApJS, 206, 7

Massaro F. et al., 2015, ApJS, 220, 5

Moderski R., Sikora M., Błażejowski M., 2003, A&A, 406, 855

Napier P. J., Bagri D. S., Clark B. G., Rogers A. E. E., Romney J. D., Thompson A. R., Walker R. C., 1994, IEEE Proc., 82, 658

Neronov A., Aharonian F. A., 2007, ApJ, 671, 85

Owen F. N., Eilek J. A., Kassim N. E., 2000, ApJ, 543, 611

Perlman E. S., Biretta J. A., Sparks W. B., Macchetto F. D., Leahy J. P., 2001, ApJ, 551, 206

Perlman E. S. et al., 2011, ApJ, 743, 119

Prieto M. A., Fernández-Ontiveros J. A., Markoff S., Espada D., González-Martín O., 2016, MNRAS, 457, 3801

Proffitt C. R., Brown T. M., Mobasher B., Davies J., 2003, Technical Report: Absolute Flux Calibration of STIS MAMA Imaging Modes. STScI, Baltimore, MA

Protheroe R. J., Clay R. W., 2004, PASA, 21, 1

Richter S., Spanier F., 2016, ApJ, 829, 56

Ryan B. R., Dolence J. C., Gammie C. F., 2015, ApJ, 807, 31

Shepherd M. C., Pearson T. J., Taylor G. B., 1994, BAAS, 26, 987

Steele I. A. et al., 2004, in Oschmann Jacobus M. J., ed., Proc. SPIE Conf. Ser. Vol. 5489, Ground-Based Telescopes. SPIE, Bellingham, p. 679

Tavecchio F., Ghisellini G., 2008, MNRAS, 385, L98

Tavecchio F., Ghisellini G., 2016, MNRAS, 456, 2374

Walker R. C., 2014, VLBA Scientific Memo n. 37. NRAO, Charlottesville, VA

Walker R. C., Hardee P. E., Davies F. B., Ly C., Junor W., 2018, ApJ, 855, 128

Waters C. Z., Zepf S. E., 2005, ApJ, 624, 656

Weidinger M., Spanier F., 2010, Int. J. Mod. Phys. D, 19, 887

Wilson A. S., Yang Y., 2002, ApJ, 568, 133

Zanin R. et al., 2013, in Shellard R. C., ed., Proc. 33rd Int. Cosmic Ray Conf (ICRC2013). Rio de Janeiro, Brazil, p. 0773 (http://inspirehep.net/record/1412925/files/icrc2013-0773.pdf)

[1]*Instituto de Astrofísica de Canarias, E-38200 La Laguna; and Departamento de Astrofísica, Universidad de La Laguna, E-38206 La Laguna, Tenerife, Spain*

[2]*Università di Udine, and INFN Trieste, I-33100 Udine, Italy*

[3]*Japanese MAGIC Consortium: ICRR, The University of Tokyo, 277-8582 Chiba, Japan; Department of Physics, Kyoto University, 606-8502 Kyoto, Japan; Tokai University, 259-1292 Kanagawa, Japan; and RIKEN, 351-0198 Saitama, Japan*

[4]*National Institute for Astrophysics (INAF), I-00136 Rome, Italy*

[5]*ETH Zurich, CH-8093 Zurich, Switzerland*

[6]*Centre for Space Research, North-West University, Potchefstroom 2520, South Africa*

[7]*INAF Osservatorio Astronomico di Padova, vicolo dell' Osservatorio 5, I-35122 Padova, Italy*

[8]*Technische Universität Dortmund, D-44221 Dortmund, Germany*

[9]*Croatian Consortium: University of Rijeka, Department of Physics, 51000 Rijeka; University of Split - FESB, 21000 Split; University of Zagreb - FER, 10000 Zagreb; University of Osijek, 31000 Osijek; and Rudjer Boskovic Institute, 10000 Zagreb, Croatia*

[10]*Saha Institute of Nuclear Physics, HBNI, 1/AF Bidhannagar, Salt Lake, Sector-1, Kolkata 700064, India*

[11]*Max-Planck-Institut für Physik, D-80805 München, Germany*

[12]*Centro Brasileiro de Pesquisas Físicas (CBPF), 22290-180 URCA, Rio de Janeiro (RJ), Brazil*

[13]*IPARCOS Institute, and EMFTEL Department, Universidad Complutense de Madrid, E-28040 Madrid, Spain*

[14]*Department of Astrophysics, University of Łódź, PL-90236 Łódź, Poland*

[15]*Università di Siena; INFN Pisa, I-53100 Siena, Italy*

[16]*Deutsches Elektronen-Synchrotron (DESY), D-15738 Zeuthen, Germany*

[17]*Università di Padova; INFN, I-35131 Padova, Italy*

[18]*Istituto Nazionale Fisica Nucleare (INFN), I-00044 Frascati (Roma), Italy*

[19]*Institut de Física d'Altes Energies (IFAE), The Barcelona Institute of Science and Technology (BIST), E-08193 Bellaterra (Barcelona), Spain*

[20]*Università di Pisa, and INFN Pisa, I-56126 Pisa, Italy*

[21]*ICRANet-Armenia at NAS RA, 0019 Yerevan, Armenia*

[22]*Centro de Investigaciones Energéticas, Medioambientales y Tecnológicas, E-28040 Madrid, Spain*

[23]*Also at Port d'Informació Científica, (PIC) E-08193 Bellaterra (Barcelona), Spain*

[24]*Universität Würzburg, D-97074 Würzburg, Germany*

[25]*Finnish MAGIC Consortium: Finnish Centre of Astronomy with ESO (FINCA), University of Turku, FI-20014 Turku; and Astronomy Research Unit, University of Oulu, FI-90014 Oulu, Finland*

[26]*Departamento de Física, and CERES-IEEC, Universitat Autònoma de Barcelona, E-08193 Bellaterra, Spain*

[27]*Also at Dipartimento di Fisica, Università di Trieste, I-34127 Trieste, Italy*

[28]*Institute for Nuclear Research and Nuclear Energy, Bulgarian Academy of Sciences, BG-1784 Sofia, Bulgaria*

[29]*Universitat de Barcelona, ICCUB, IEEC-UB, E-08028 Barcelona, Spain*

[30]*Also at INAF-Trieste, I-34143 Trieste; and Department of Physics and Astronomy, University of Bologna, I-40127 Bologna, Italy*

[31]*ICRR, University of Tokyo, Kashiwa-shi, Chiba 277-8582, Japan*

[32]*Mizusawa VLBI Observatory, National Astronomical Observatory of Japan, 2-12 Hoshigaoka-cho, Mizusawa, Oshu, Iwate 023-0861, Japan*

[33]*Department of Astronomical Science, The Graduate University for Advanced Studies (SOKENDAI), 2-21-1 Osawa, Mitaka, Tokyo 181-8588, Japan*

[34]*Smithsonian Astrophysical Observatory, 60 Garden Street, Cambridge, MA 02138, USA*

[35]*INAF Istituto di Radioastronomia, via Gobetti 101, I-40129 Bologna, Italy*

[36]*Astrophysics Research Institute, Liverpool John Moores University, Liverpool L1 2U, UK*

[37]*Department of Physics and Astronomy, University of Texas Rio Grande Valley, One West University Blvd., Brownsville, TX 78520, USA*

[38]*Dipartimento di Fisica, Università degli Studi di Torino, via Pietro Giuria 1, I-10125 Torino, Italy*

[39]*INFN, Sezione di Torino, I- 10125 Torino, Italy*

[40]*INAF-Osservatorio Astrofisico di Torino, via Osservatorio 20, I-10025 Pino Torinese, Italy*

[41]*Consorzio Interuniversitario per la Fisica Spaziale (CIFS), via Pietro Giuria 1, I-10125 Torino, Italy*

[42]*Institut für Theoretische Astrophysik, Universität Heidelberg, D-69120 Heidelberg, Germany*

[43]*National Radio Astronomy Observatory, Socorro, NM 87801, USA*

This paper has been typeset from a TeX/LaTeX file prepared by the author.